Neuron
Article

Nonlinear Regulation of Unitary Synaptic Signals by $CaV_{2.3}$ Voltage-Sensitive Calcium Channels Located in Dendritic Spines

Brenda L. Bloodgood[1] and Bernardo L. Sabatini[1,*]
[1] Department of Neurobiology, Harvard Medical School, Boston, MA 02115, USA
*Correspondence: bsabatini@hms.harvard.edu
DOI 10.1016/j.neuron.2006.12.017

SUMMARY

The roles of voltage-sensitive sodium (Na) and calcium (Ca) channels located on dendrites and spines in regulating synaptic signals are largely unknown. Here we use 2-photon glutamate uncaging to stimulate individual spines while monitoring uncaging-evoked excitatory postsynaptic potentials (uEPSPs) and Ca transients. We find that, in CA1 pyramidal neurons in acute mouse hippocampal slices, $CaV_{2.3}$ voltage-sensitive Ca channels (VSCCs) are found selectively on spines and act locally to dampen uncaging-evoked Ca transients and somatic potentials. These effects are mediated by a regulatory loop that requires opening of $CaV_{2.3}$ channels, voltage-gated Na channels, small conductance Ca-activated potassium (SK) channels, and NMDA receptors. Ca influx through $CaV_{2.3}$ VSCCs selectively activates SK channels, revealing the presence of functional Ca microdomains within the spine. Our results suggest that synaptic strength can be modulated by mechanisms that regulate voltage-gated conductances within the spine but do not alter the properties or numbers of synaptic glutamate receptors.

INTRODUCTION

Voltage-gated and calcium (Ca)-dependent channels in dendrites of pyramidal neurons support the propagation of somatic action potentials (APs) and determine features of the AP such as the afterhyperpolarization and afterdepolarization (Magee, 1999; Metz et al., 2005; Stocker et al., 1999). Voltage-sensitive Ca channels (VSCCs) within dendrites and dendritic spines also mediate back-propagating AP- (bAP) evoked Ca transients and allow generation of dendritic Ca spikes (Golding et al., 2002; Sabatini and Svoboda, 2000; Wei et al., 2001; Yuste and Denk, 1995). However, the roles of these channels in shaping synaptic signals, such as synaptic potentials and spine head Ca transients, remain largely unknown.

Following synaptic stimulation, voltage- and Ca-gated ion channels can only open secondarily as a consequence of the activation of other channels that provide the depolarization or Ca influx necessary for gating. Therefore, any influence they have on synaptically evoked potentials and Ca transients results from a cascade of ion channel opening. Several such regulatory loops have been identified in which synaptic depolarization or Ca influx activates ion channels that feed back to modulate excitability. First, small-conductance Ca-activated potassium (SK) channels located on the spine head are opened by stimulation of the associated synapse (Ngo-Anh et al., 2005). This dampens Ca influx through NMDA-type glutamate receptors (NMDARs) by repolarizing the membrane and promoting Mg block of NMDARs. For this reason, blockade of SK channels with the peptide toxin apamin enhances NMDAR-dependent Ca influx and facilitates induction of long-term potentiation (LTP). Second, stimulation of distal synapses in hippocampal pyramidal neurons modulates hyperpolarization-activated cationic channels that mediate the current referred to as I_h. These channels reduce the input resistance of dendrites and accelerate the kinetics of excitatory postsynaptic potentials (EPSP) (Hoffman et al., 1997; Magee et al., 1998; Magee, 1999). Third, activation of transient type-A potassium channels, or I_A, may counterbalance voltage-gated sodium (Na) channels (VGSCs) opened by synaptic potentials and thus prevent generation of dendritic APs (Hoffman et al., 1997).

The involvement of voltage-gated Ca and Na channels in shaping synaptic signals has been more difficult to determine. Since activation of these channels is necessary for AP-evoked presynaptic release of neurotransmitter, combining conventional electrophysiological and pharmacological techniques to probe their involvement in postsynaptic signaling is not possible. Furthermore, some voltage-gated Ca channels are found within dendritic spines, and their roles in locally shaping electrical and biochemical signals evoked by synaptic stimulation may not be detectable in somatic electrophysiological recordings.

Here we examine the classes of VSCCs present in proximal dendrites and dendritic spines of mouse CA1 pyramidal neurons and their contribution to synaptic potentials

and spine head Ca transients. We avoid the technical obstacles discussed above by using 2-photon laser photoactivation (2PLP) of caged glutamate to bypass the presynaptic terminal and deliver a stimulus of standard amplitude. This approach is combined with imaging of dendritic Ca transients by 2-photon laser-scanning microscopy (2PLSM) and whole-cell recording of somatic potentials to measure the responses evoked by stimulation of a single, visualized spine. We find that multiple classes of VSCCs are active in secondary and tertiary apical dendrites, but that these classes differ between the dendritic shaft and dendritic spines. $CaV_{2.3}$ VSCCs are specifically located in the spine head, where they nonlinearly regulate synaptic signaling. The net effect of blockade of $CaV_{2.3}$ VSCCs with the peptide toxin SNX-482 (SNX) is to increase synaptically evoked potentials and spine head Ca transients. By examining these signals with combinations of ion channel antagonists, we demonstrate that Ca influx through $CaV_{2.3}$ VSCCs has a privileged role in activating SK channels and regulating NMDAR-dependent Ca influx, revealing the existence of functional Ca microdomains within the spine. Our study demonstrates that synaptic signals are regulated by a multistep regulatory loop that is activated in individual spines by single stimuli. This feedback loop requires large local swings in membrane potential and activation of VGSCs, $CaV_{2.3}$ VSCCs, SK channels, and NMDARs.

RESULTS

Synaptic Ca Signals Are Mediated by NMDARs and VSCCs

Whole-cell recordings were made from CA1 pyramidal neurons in acute hippocampal slices prepared from juvenile (postnatal day 15–18, or P15–P18) C57/Blk6 mice. Cells were filled through the patch pipette with the Ca-sensitive, green-fluorescing fluorophore Fluo-5F (300 μM) and the Ca-independent, red-fluorescing fluorophore Alexa Fluor 594 (10 μM), and the fluorescence of both fluorophores was imaged with 2PLSM. Red fluorescence was used to visualize the cellular morphology and to identify spines within the proximal 150 μm of apical dendrite (Figure 1). Neurons were transiently held in voltage-clamp and the position of the spot of 2PLP-mediated glutamate uncaging was systematically varied around the periphery of the spine to determine the location that produced the maximal uncaging-evoked excitatory postsynaptic current (uEPSC). Laser power was subsequently adjusted such that a 500 μs laser pulse directed at this optimal position elicited a 10–15 pA uEPSC. The amplifier was switched to current-clamp for the remainder of the analysis. Uncaging-evoked fluorescence transients were monitored in line scan mode in the spine head and adjacent dendrite while uncaging-evoked excitatory postsynaptic potentials (uEPSPs) were recorded at the soma (Figure 1B). Fluorescence transients were quantified relative to maximal green fluorescence at saturating levels of Ca ($\Delta G_{uEPSP}/G_{sat}$), a measure that, because of the high concentration of low-affinity indicator used, is linearly proportional to evoked changes in Ca ($\Delta[Ca]_{uEPSP}$).

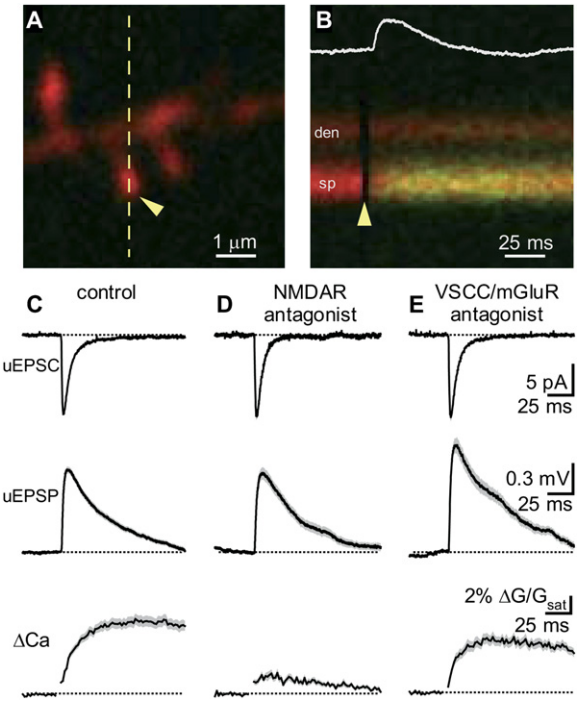

Figure 1. NMDARs and VSCCs Regulate Uncaging-Evoked Potentials and Spine Head Ca Transients

(A) 2PLSM image of a spiny region of an apical dendrite of a CA1 hippocampal pyramidal neuron filled with 10 μM Alexa 594 (red fluorescence) and 300 μM of the Ca indicator Fluo-5F (green fluorescence).

(B) Fluorescence collected in a line scan, as indicated by the dashed line in (A), that intersects the spine head (sp) and neighboring dendrite (den) during glutamate uncaging onto the spine head. The arrowheads in (A) and (B) indicate the location and timing, respectively, of a 500 μs pulse of 725 nm laser light used to trigger 2-photon mediated photolysis of MNI-glutamate. The increase in green fluorescence indicates increased intracellular [Ca]. The white trace shows the uEPSP (amplitude 0.59 mV) recorded simultaneously at the soma.

(C) uEPSC (top), uEPSP (middle), and $\Delta G_{uEPSP}/G_{sat}$ (bottom) measured in control conditions. In this and all subsequent figures, the solid line and shaded regions depict the average ± the standard error of the mean (SEM), respectively. In this and all figures depicting uncaging-evoked spine head Ca transients at room temperature, 1% $\Delta G/G_{sat}$ corresponds to 11 nM Δ[Ca] (see Experimental Procedures).

(D) uEPSC (top), uEPSP (middle), and $\Delta G_{uEPSP}/G_{sat}$ (bottom) measured in the presence of NMDAR antagonists (20 μM CPP and 40 μM MK-801).

(E) uEPSC (top), uEPSP (middle), and $\Delta G_{uEPSP}/G_{sat}$ (bottom) measured in the presence of VSCC and mGluR antagonists (20 μM nimodipine, 1 μM CTX-MVIIC, 0.3 μM SNX, 10 μM mibefradil, 1 μM MPEP, 100 μM CPCCOEt).

In control conditions, this stimulation protocol resulted in a uEPSC of −12.53 ± 0.27 pA and a uEPSP of 0.83 ± 0.04 mV (n = 77/59 spines/cells) (Figure 1C). These amplitudes are in the upper range of those of miniature synaptic currents and potentials generated from similar proximal regions of the dendrite (Losonczy and Magee, 2006;

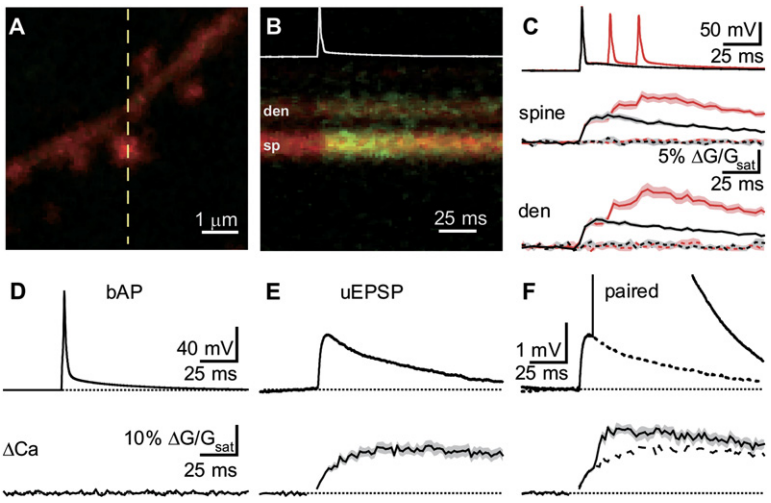

Figure 2. A Cocktail of VSCC Antagonists Prevents bAP-Evoked Ca Transients in Spines and Dendrites without Precluding bAP Propagation

(A) Image of a spiny apical dendrite filled with 5 μM Alexa 594 (red fluorescence) and 150 μM Fluo-5F (green fluorescence).

(B) Fluorescence collected in a line scan as indicated in (A) that intersects the spine head (sp) and neighboring dendrite (den) during stimulation of a bAP by somatic current injection. A bAP (white trace) rapidly increases green fluorescence in the spine and dendrite, indicating increased [Ca] in both compartments.

(C) Quantification of the fluorescence transients ($\Delta G_{bAP}/G_{sat}$) in the spine head (middle) and neighboring dendrite (bottom) evoked by 1 (black) or 3 (red) bAPs (top). $\Delta G_{bAP}/G_{sat}$ was recorded in control conditions (solid lines) and in the presence of a VSCC antagonist cocktail (dashed lines) consisting of 20 μM nimodipine, 1 μM CTX-MVIIC, 0.3 μM SNX, and 10 μM mibefradil.

(D–F) Membrane potentials (top) and spine head fluorescence transients (bottom) evoked by a bAP (D), a uEPSP (E), and a uEPSP/bAP pair (F) in the presence of VSCC antagonists. In the right panel, the uEPSP and the uEPSP-evoked Ca transient from (E) are replotted (dashed line) for comparison.

Magee and Cook, 2000). The uEPSP was accompanied by a fluorescence transient in the spine head, indicative of Ca entry, of amplitude 8.5% ± 0.7%. Using this standard uncaging stimulus, the coefficient of variation of the uEPSC, uEPSP, and $\Delta G_{uEPSP}/G_{sat}$ were 29%, 39%, and 57%, respectively, allowing for the detection of ~10% variability about the mean using information from 20–30 spines (see Figure S1 in the Supplemental Data). In the experiments that are described below, unless otherwise specified, comparisons are made across conditions using data pooled from ~20 spines collected in the continuous presence of the specified drugs.

Recordings (uEPSC = −13.20 ± 0.47 pA; n = 24/11 spines/cells) obtained in the presence of NMDAR antagonists CPP and MK-801 revealed a similar uEPSP (0.80 ± 0.06 mV) but greatly reduced $\Delta[Ca]_{uEPSP}$ ($\Delta G_{uEPSP}/G_{sat}$ = 1.3% ± 0.3%) (Figure 1D), consistent with a prominent contribution of Ca influx through NMDARs to synaptically evoked Ca transients in the spine head (Mainen et al., 1999; Oertner et al., 2002; Yuste and Denk, 1995). To determine if other Ca sources also play a role in shaping spine head Ca transients, recordings were repeated in the presence of a cocktail of antagonists of metabotropic glutamate receptors (mGluRs) and VSCCs consisting of CPCCOEt, MPEP, nimodipine, ω-conotoxin-MVIIC (CTX-MVIIC), SNX, and mibefradil (Figure 1E). These agents target, respectively, mGluR1 and mGluR5 as well as $CaV_{1.2/1.3}$ (L-type), $CaV_{2.1/2.2}$ (P/Q- and N-type), $CaV_{2.3}$ (R-type), and CaV_3 (T-type) classes of VSCCs. We avoided using broad-spectrum divalent (Cd^{+2} and Ni^{+2}) antagonists of VSCCs as these may enter the cell and bind to the Ca indicator (Hinkle et al., 1992; Regehr and Atluri, 1995) and may also perturb the opening and conductance of NMDAR (Westbrook and Mayer, 1987; Legendre and Westbrook, 1990). In the presence of these antagonists, the same uncaging stimulus (uEPSC = −12.84 ± 0.66 pA; n = 25/18 spines/cells) resulted in a ~29% larger uEPSP (1.07 ± 0.08 mV, $p < 0.05$) and ~28% smaller $\Delta[Ca]_{uEPSP}$ ($\Delta G_{uEPSP}/G_{sat}$ = 6.1% ± 0.5%, $p < 0.05$) (Figure 1E) compared with control conditions. These results indicate that the net result of activation of non-NMDAR Ca sources is a boost of spine head Ca transients and a dampening of synaptic potentials.

Multiple VSCC Subclasses Are Found in Dendrites and Dendritic Spines

In order to determine which subclasses of VSCCs are present in proximal apical spines and dendrites that might contribute to the regulation of synaptic signals, we used pharmacological analysis of bAP-evoked Ca transients ($\Delta[Ca]_{bAP}$) (Johnston et al., 1992; Sabatini and Svoboda, 2000; Yuste and Denk, 1995) (Figure 2). 2PLSM was used as above to identify spines for analysis (Figure 2A) and to measure bAP-evoked fluorescence transients in the spine head and neighboring dendrite (Figure 2B). In order to accurately monitor the small bAP-evoked fluorescence transients ($\Delta G_{bAP}/G_{sat}$), the concentrations of Fluo-5F and Alexa 594 were decreased to 150 and 5 μM, respectively. Furthermore, in order to eliminate a Ca-dependent conductance known to be present in dendritic spines (Ngo-Anh et al., 2005) that might complicate the analysis of $\Delta[Ca]_{bAP}$, SK channels were blocked with apamin (100 nM). In these conditions, somatic depolarization triggers an AP that invades proximal apical dendrites and spines and results in a fluorescence transient in both structures (Figure 2B). Because of the strong barrier to diffusional equilibration that is posed by the spine neck, the magnitude of the fluorescence transients measured in the spine or dendrite immediately after the bAP reflects Ca influx directly into each structure. Under our recording

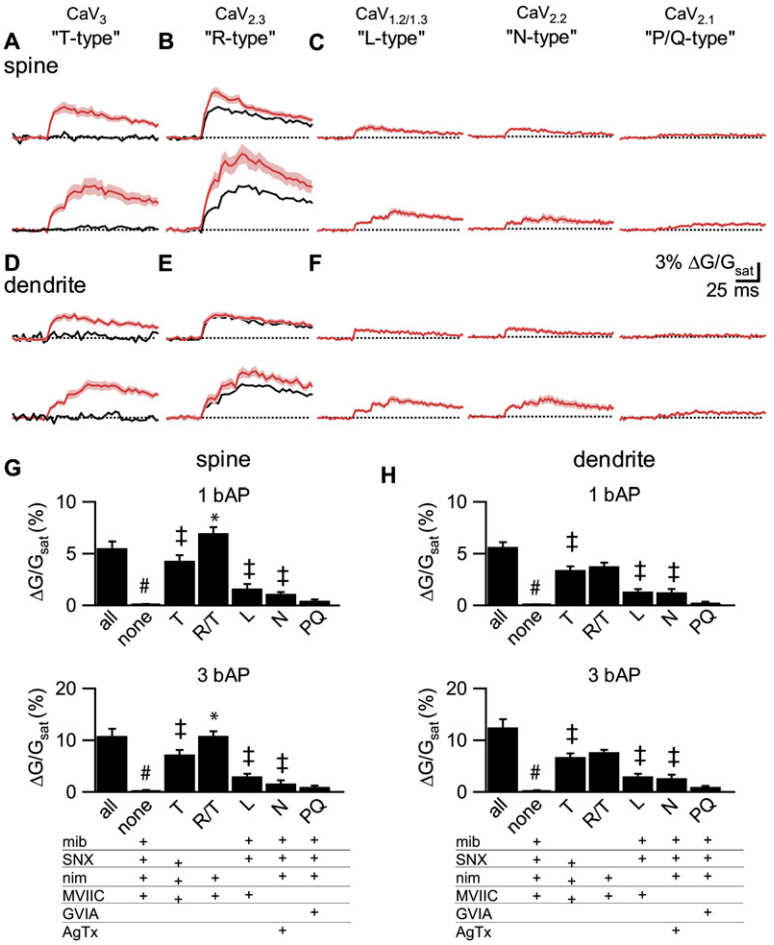

Figure 3. Multiple and Distinct Sets of VSCC Classes Contribute to bAP-Mediated Ca Transients in Spines and Dendrites

(A) $\Delta G_{bAP}/G_{sat}$ evoked by a single bAP (top) or a trio of bAPs (bottom, 50 Hz) measured in spines in the presence of nimodipine, CTX-MVIIC, and SNX (red traces) or in the additional presence of mibefradil (black traces). The latter data is replotted from Figure 2B. This pharmacological profile is representative of T-type, CaV_3 VSCCs.

(B) $\Delta G_{bAP}/G_{sat}$ evoked in the spine head by a single bAP (top) or a trio of bAPs (bottom) in the presence of nimodipine and CTX-MVIIC to isolate R/T-type VSCCs (red traces). In both panels comparison is made with the isolated T-type data from (A) (black traces). The difference between the black and red lines represents the additional Ca influx resulting from activation of $CaV_{2.3}$ VSCCs.

(C) $\Delta G_{bAP}/G_{sat}$ evoked by a single bAP (top, red trace) or a trio of bAPs (bottom, red trace) in the spine head in the presence of CTX-MVIIC, SNX, and mibefradil (left); nimodipine AgTx, SNX, and mibefradil (middle); or nimodipine CTX-GVIA, SNX, and mibefradil (right) to isolate $CaV_{1.2/1.3}$, $CaV_{2.2}$, and $CaV_{2.1}$ VSCCs, respectively.

(D–F) As in (A–C) for bAP-evoked fluorescence transients measured from the dendrites immediately adjacent to the analyzed spines.

(G) Summary of the relative amplitudes of bAP-evoked Ca transients measured in spines in response to a single bAP (top) or a trio of bAPs (bottom) for each of the pharmacological conditions shown in (A–C).

(H) As in panel (G) for bAP-evoked Ca transients measured in the dendrite (D–F). (#), (‡), and (*) indicate statistically significant ($p < 0.05$) differences compared with control, all VSCC blockers, or isolated T-type conditions, respectively.

conditions, the average time of fluorophore equilibration across the spine neck is >100 ms (Figure S3A) (Majewska et al., 2000; Sabatini et al., 2002).

Quantification of $\Delta G_{bAP}/G_{sat}$ evoked by a single (n = 20/14 spines/cells) bAP or trio (n = 11/7 spines/cells) of bAPs at 50 Hz reveals that the Ca increases in both structures are fully blocked by the VSCC antagonist cocktail of nimodipine, CTX-MVIIC, SNX, and mibefradil (Figure 2C) (n = 11/7 and 7/4 spines/cells for 1 and 3 bAPs, respectively). In order to confirm that the blockade of $\Delta[Ca]_{bAP}$ was due to antagonism of VSCCs in the dendrite and spine, and not due to failure of dendritic propagation of the AP, we examined the effects of bAPs on $\Delta[Ca]_{uEPSP}$ in the presence of the VSCC antagonist cocktail (Figures 2D–2F). Under these conditions, $\Delta[Ca]_{bAP}$ was not detectable (Figure 2D; $\Delta G_{bAP}/G_{sat}$ = 0.03% ± 0.07%; n = 7/3 spines/cells), whereas in the same spines, $\Delta[Ca]_{uEPSP}$ was maintained (Figure 2E; $\Delta G_{uEPSP}/G_{sat}$ = 14.5% ± 1.7%) and enhanced when paired with a bAP (delay of 10 ms) (Figure 2F; $\Delta G_{pair}/G_{sat}$ = 19.8% ± 1.7%, $p < 0.05$). This boosting is consistent with increased NMDAR-dependent Ca influx due to bAP-mediated relief of Mg block (Nevian and Sakmann, 2004; Yuste and Denk, 1995), indicating that AP propagation into proximal apical dendrites and spines does not require VSCCs.

bAP-evoked Ca influx through individual VSCC subclasses was isolated by removing components of the VSCC-antagonist cocktail (Figure 3). Removal of mibefradil from the cocktail significantly increased $\Delta[Ca]_{bAP}$ in the spine head and dendrite relative to measurements performed in the presence of the full cocktail (Figures 3A and 3D) for both a single bAP and a trio (n = 30/15 spines/cells) of bAPs. Because of the continued presence of nimodipine, SNX, and CTX-MVIIC, specific $CaV_{1.2/1.3}$, $CaV_{2.3}$, and $CaV_{2.1/2.2}$ antagonists, respectively, this component can be attributed to the opening of mibefradil-sensitive CaV_3 (T-type) VSCCs. Since mibefradil and low concentrations of Ni^{2+}, the most specific antagonists of

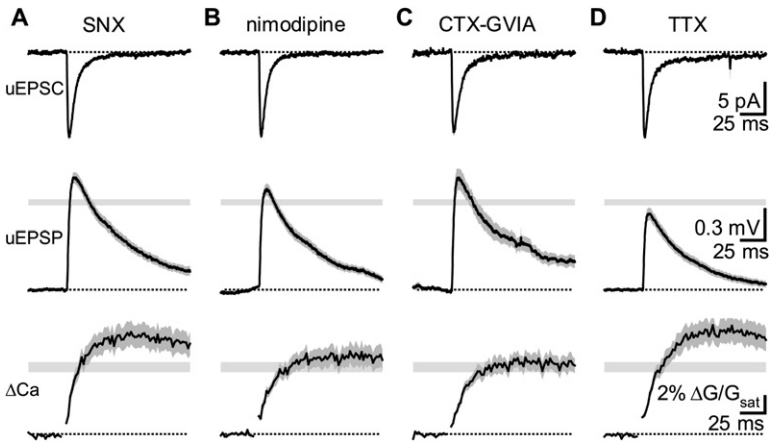

Figure 4. Differential Regulation of uEPSP and $\Delta[Ca]_{uEPSP}$ by Voltage-Sensitive Ca and Na Channels

uEPSC (top), uEPSP (middle), and $\Delta G_{uEPSP}/G_{sat}$ (bottom) measured in the presence of antagonists of $CaV_{2.3}$ (SNX) (A), $CaV_{1.2/1.3}$ (nimodipine) (B), $CaV_{2.2}$ (CTX-GVIA) (C), or voltage-gated Na channels (TTX) (D). In the lower panels, the range of amplitudes (± SEM) of the uEPSP and $\Delta G_{uEPSP}/G_{sat}$ measured in control conditions are shown by the gray shaded bars.

CaV_3 VSCCs (McDonough and Bean, 1998), also inhibit $CaV_{2.3}$ (Randall and Tsien, 1997), it is not possible to isolate Ca influx through $CaV_{2.3}$ channels independently of CaV_3 Ca channels. Comparison of $\Delta[Ca]_{bAP}$ with both $CaV_{2.3}$ and CaV_3 channels active, measured in the presence of nimodipine and CTX-MVIIC (n = 22/11 spines/cells), to that measured with only CaV_3 channels active reveals an additional increase due to the opening of $CaV_{2.3}$ in the spine (Figure 3B) but not in the adjacent dendrite (Figure 3E). Similarly, $\Delta[Ca]_{bAP}$ was measured in the presence of the following: CTX-MVIIC, SNX, and mibefradil to isolate $CaV_{1.2/1.3}$ (n = 11/3 spines/cells); nimodipine, SNX, ω-agatoxin-IVA (AgTx), and mibefradil to isolate $CaV_{2.2}$ (n = 12/6 spines/cells); and nimodipine, SNX, ω-conotoxin-GVIA (CTX-GVIA), and mibefradil to isolate $CaV_{2.1}$ (n = 17/6 spines/cells) (Figures 3C and 3F). Significant Ca influx through isolated $CaV_{1.2/1.3}$ and $CaV_{2.2}$ VSCCs was observed in both the spine head and neighboring dendrite, whereas $CaV_{2.1}$ VSCCs did not contribute significantly to $\Delta[Ca]_{bAP}$ in either compartment (Figures 3C and 3F). These data demonstrate that $CaV_{2.3}$ VSCCs are located in spines, but not in the adjacent dendrite, whereas $CaV_{1.2/1.3}$ and $CaV_{2.2}$ VSCCs are in both compartments, while $CaV_{2.1}$ VSCCs are in neither.

Synaptic Activation of VSCCs

Since $CaV_{2.3}$ VSCCs are selectively present in dendritic spines, we hypothesized that this channel may play a role in regulating synaptic signaling. To test this idea, $\Delta[Ca]_{uEPSP}$ and the uEPSP were measured in the presence of selective VSCC antagonists (Figure 4). In the presence of the $CaV_{2.3}$ antagonist SNX, our standard stimulus (uEPSC = −12.45 ± 0.47 pA; n = 28/13 spines/cells) generated a larger uEPSP (1.17 ± 0.06 mV, $p < 0.05$) and $\Delta[Ca]_{uEPSP}$ ($\Delta G_{uEPSP}/G_{sat}$ = 12.1% ± 1.2%, $p < 0.05$) than in control conditions (Figure 4A). Since *blocking* this Ca source *increased* Ca accumulation in the spine, $CaV_{2.3}$ VSCCs must nonlinearly regulate Ca influx through other uEPSP-activated Ca channels. In contrast, application of nimodipine had no effect on evoked signals (uEPSC = −12.83 ± 0.42 pA; uEPSP = 0.98 ± 0.06 mV; $\Delta G_{uEPSP}/G_{sat}$ = 8.9% ± 0.9%; n = 23/11 spines/cells) (Figure 4B), whereas CTX-GVIA increased the amplitude of the uEPSP (uEPSC = −12.57 ± 0.61 pA; uEPSP = 1.09 ± 0.10 mV; n = 15/6 spines/cells, $p < 0.05$) with no effects on $\Delta[Ca]_{uEPSP}$ ($\Delta G_{uEPSP}/G_{sat}$ = 8.2% ± 0.8%) (Figure 4C). To examine if VGSCs also regulate synaptic signals, the standard stimulus (uEPSC = −12.54 ± 0.42 pA; n = 22/9 spines/cells) was delivered in the presence of the VGSC antagonist tetrodotoxin (TTX). Blockade of VGSCs did not affect the amplitude of the uEPSP (0.74 ± 0.06 mV), but did enhance $\Delta[Ca]_{uEPSP}$ ($\Delta G_{uEPSP}/G_{sat}$ = 11.6% ± 1.3%; $p < 0.05$) (Figure 4D). Thus, as demonstrated by the differential effects of SNX, CTX-GVIA, and TTX on the uEPSP and on $\Delta[Ca]_{uEPSP}$, synaptic potentials and spine head Ca transients are separately and nonlinearly regulated by the action of multiple voltage-gated ion channels.

$CaV_{2.3}$ and VGSCs Regulate Synaptic Signals by Activating SK Channels in the Spine

The effects of $CaV_{2.3}$ blockade on uEPSP and $\Delta[Ca]_{uEPSP}$ are similar to those seen following blockade of SK channels with the peptide antagonist apamin (Ngo-Anh et al., 2005). To determine if apamin and antagonists of voltage-sensitive conductances affect synaptic signals through a common mechanism, the effects of apamin on the uEPSP and $\Delta[Ca]_{uEPSP}$ were examined in a variety of conditions (Figure 5). As reported previously (Ngo-Anh et al., 2005), and as reproduced here in a new data set, standard stimulation (uEPSC = −12.58 ± 0.43 pA; n = 31/21 spines/cells) in the presence of apamin increases the uEPSP (1.01 ± 0.07 mV; $p < 0.05$) and $\Delta[Ca]_{uEPSP}$ ($\Delta G_{uEPSP}/G_{sat}$ = 10.9% ± 1.0%; $p < 0.05$) relative to control (Figure 5A). Furthermore, as reported previously, application of apamin has no effect on evoked signals when NMDARs are blocked with CPP/MK-801 (uEPSC = −12.62 ± 0.53 pA; uEPSP = 0.91 ± 0.07 mV; $\Delta G_{uEPSP}/G_{sat}$ = 1.2% ± 0.2% in the presence of apamin and NMDAR antagonists; n = 24/16 spines/cells) (Figure 5B). Thus, activation of NMDARs is necessary for the apamin-mediated boost of uEPSP and $\Delta[Ca]_{uEPSP}$. To determine if they are sufficient,

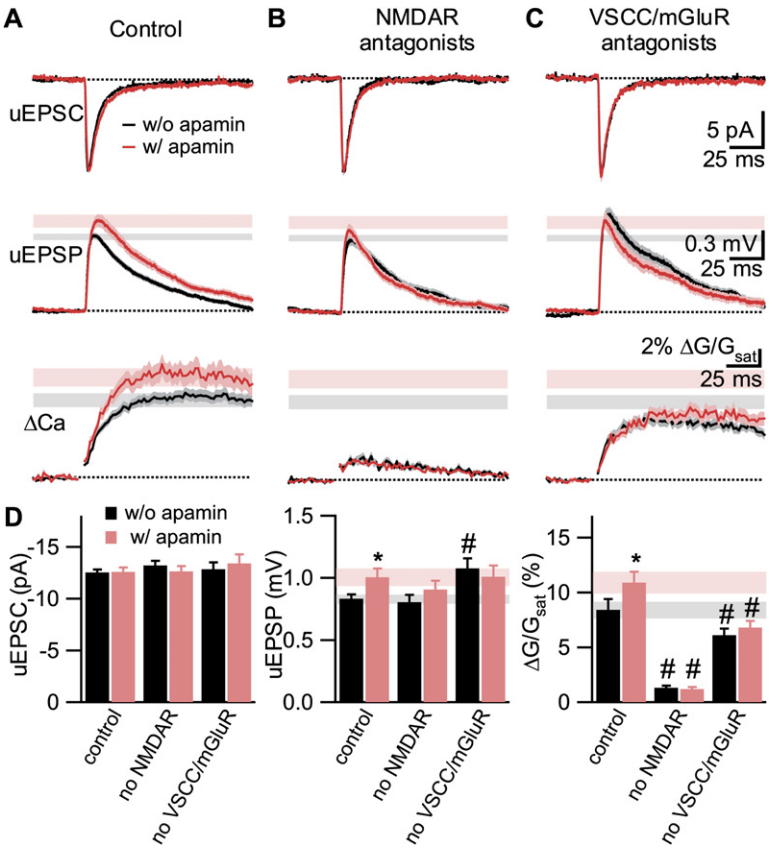

Figure 5. NMDARs Are Necessary but Not Sufficient for the Action of SK Channels on the uEPSP and $\Delta[Ca]_{uEPSP}$

(A) uEPSC (top), uEPSP (middle), and $\Delta G_{uEPSP}/G_{sat}$ (bottom) measured in control conditions (black traces) and in the presence of the SK channel antagonist apamin (red traces).

(B) uEPSC (top), uEPSP (middle), and $\Delta G_{uEPSP}/G_{sat}$ (bottom) measured in the presence of NMDAR antagonists (black traces; CPP/MK-801) or in the additional presence of apamin (red traces; CPP/MK-801/apamin).

(C) uEPSC (top), uEPSP (middle), and $\Delta G_{uEPSP}/G_{sat}$ (bottom) measured in the presence of VSCC and mGluR antagonists (black traces; nimodipine/CTX-MVIIC/SNX/mibefradil/CPCCOEt/MPEP) or in the additional presence of apamin (red traces).

(D) Summary of the amplitudes of the uEPSC (left), uEPSP (middle), and $\Delta G_{uEPSP}/G_{sat}$ (right) in each pharmacological condition. In the lower panels of (A–C) and in (D), the shaded bars indicate the range of amplitudes (±SEM) for the uEPSP or $\Delta G_{uEPSP}/G_{sat}$ in control conditions (gray) or in the presence of apamin (pink) alone. For conditions lacking apamin, (#) indicates $p < 0.05$ compared with control conditions. For apamin-containing conditions, (#) indicates $p < 0.05$ compared with apamin alone. (*) indicates $p < 0.05$ for each apamin condition compared with the corresponding apamin-free condition.

we examined the effects of apamin in the presence of the VSCC/mGluR antagonist cocktail. In this condition, the presence or absence of apamin had no effect on the uEPSP or on $\Delta[Ca]_{uEPSP}$ (uEPSC = −13.40 ± 0.88. pA; uEPSP = 1.01 ± 0.09 mV; $\Delta G_{uEPSP}/G_{sat}$ = 6.3% ± 0.5% in the presence of apamin and VSCC/mGluR antagonists; n = 16/11 spines/cells) (Figure 5C). Thus, the effects of apamin on uEPSP and $\Delta[Ca]_{uEPSP}$ require the activity of both NMDARs and a second Ca source (Figure 5D).

To determine if the opening of a specific voltage-sensitive channel is necessary for SK channel activation, the uEPSP and $\Delta[Ca]_{uEPSP}$ were measured with a combination of apamin and antagonists of voltage-gated ion channels (Figure 6). In the presence of apamin and SNX, the standard stimulation (uEPSC = −12.86 ± 0.56 pA; n = 23/17 spines/cells) resulted in uEPSP (1.13 ± 0.11 mV) and $\Delta[Ca]_{uEPSP}$ ($\Delta G_{uEPSP}/G_{sat}$ = 11.3% ± 1.1%) measurements that were the same as those recorded in SNX or apamin alone (Figure 6A), indicating that blockade of $CaV_{2.3}$ occludes the normal SK-mediated inhibition of the uEPSP and $\Delta[Ca]_{uEPSP}$. In contrast, coapplication of nimodipine and apamin caused a significant increase in the uEPSP (uEPSC = −12.28 ± 0.39 pA; uEPSP = 1.20 ± 0.09 mV; n = 26/12 spines/cells; $p < 0.05$) and a slight increase in $\Delta[Ca]_{uEPSP}$ ($\Delta G_{uEPSP}/G_{sat}$ = 10.4% ± 1.4%) compared with nimodipine alone (Figure 6B). Coapplication of apamin and CTX-GVIA (uEPSC = −13.20 ± 0.51; n = 14/6 spines/cells) significantly increased the uEPSP (1.37 ± 0.08 mV, $p < 0.05$) and $\Delta[Ca]_{uEPSP}$ ($\Delta G_{uEPSP}/G_{sat}$ = 15.7% ± 1.4%, $p < 0.05$) (Figure 6C) relative to CTX-GVIA alone. Lastly, signals measured in the presence of TTX and apamin (uEPSC = −12.15 ± 0.51 pA; uEPSP = 0.68 ± 0.05 mV; $\Delta G_{bAP}/G_{sat}$ = 10.6% ± 0.9%; n = 18/10 spines/cells) (Figure 6D) were the same as those measured in the presence of TTX alone, indicating that the opening of VGSCs is also necessary for SK-dependent modulation of the uEPSP and $\Delta[Ca]_{uEPSP}$.

Normalization of Laser Power Delivered to the Spine

In the experiments described above, laser power was adjusted to evoke a uEPSC of standard amplitude at the soma. However, changes in the space constant or resting conductance of the dendrite across pharmacological conditions may alter the ability to voltage clamp the spine and may introduce systematic differences in the uncaging laser power and uncaged glutamate concentration used to achieve the standard uEPSC. For this reason, we developed an alternative approach in which photobleaching of the red fluorophore in the spine of interest was used to set laser power (see Supplemental Experimental Procedures) (Figure 7). This method is independent of the electrophysiological state of the cell, the microscope under which the experiment is performed, and many optical variables, such as the power of the imaging laser, concentration of

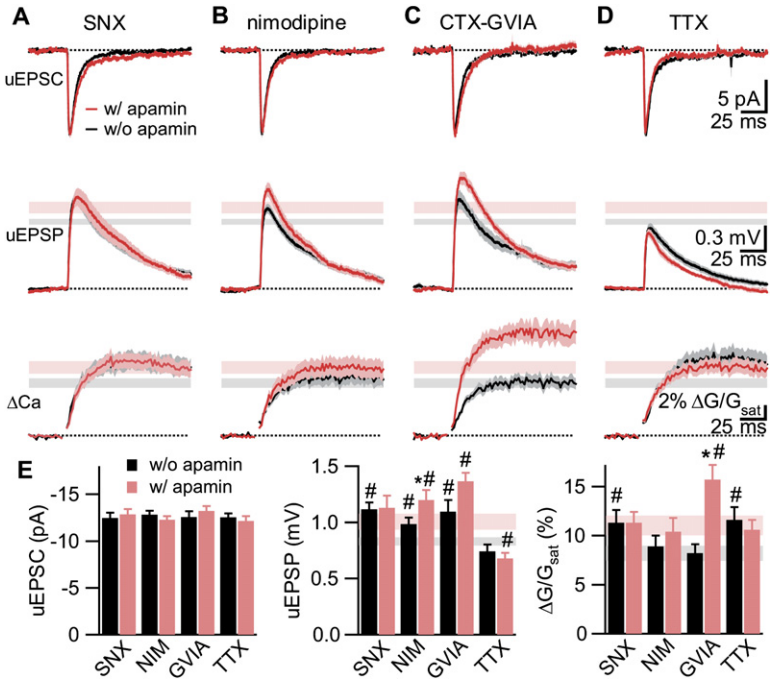

Figure 6. The Activities of $CaV_{2.3}$ VSCCs and VGSCs Are Necessary for SK-Dependent Modulation of Synaptic Potentials and Spine Head Ca Transients

(A) uEPSC (top), uEPSP (middle), and $\Delta G_{uEPSP}/G_{sat}$ (bottom) measured in the presence of antagonists of $CaV_{2.3}$ (black traces, SNX) or $CaV_{2.3}$ and SK channels (red traces, SNX/apamin).

(B) As in (A), but in the presence of antagonists of $CaV_{1.2/1.3}$ (black traces, nimodipine) or $CaV_{1.2/1.3}$ and SK channels (red traces, nimodipine/apamin).

(C) As in (A), but in the presence of antagonists of $CaV_{2.2}$ (black traces, CTX-GVIA) or $CaV_{2.2}$ and SK channels (red traces, CTX-GVIA/apamin).

(D) As in (A), but in the presence of antagonists of VGSCs (black traces, TTX) or VGSCs and SK channels (red traces, TTX/apamin).

(E) Summary of amplitudes of the uEPSC (left), uEPSP (middle), and $\Delta G_{uEPSP}/G_{sat}$ (right) in each condition. In the lower panels of (A–D) and in (E), the shaded bars indicate the range of amplitudes (±SEM) for the uEPSP or $\Delta G_{uEPSP}/G_{sat}$ in control conditions (gray) or in the presence of apamin alone (pink). For conditions lacking apamin, (#) indicates $p < 0.05$ compared with control ACSF. For apamin-containing conditions, (#) indicates $p < 0.05$ compared with apamin alone. (*) indicates $p < 0.05$ for each apamin condition compared with the corresponding apamin-free condition.

the red fluorophore, depth of the spine in the slice, and local inhomogeneity in the index of refraction.

Recordings in control neurons indicated that to obtain a 10–15 pA uEPSC with a 500 μs laser pulse requires power that bleaches ~40% of the Alexa 594 fluorescence in the spine head (Figure 7B) (uEPSC = −12.79 ± 0.46 pA and $\Delta R/R_0$ = 42.13% ± 4.5%, n = 20/4 spines/cells). Therefore, in subsequent experiments, for each spine of interest, the uncaging laser was first directed at the spine head and power was adjusted such that a 500 μs pulse bleached ~40% of the red fluorescence. The uncaging position was then systematically varied around the periphery of the spine to determine the location that produced the maximal electrical response. Uncaging at this position was used without changing laser power, and uncaging-evoked fluorescence transients in the spine head and uEPSPs at the soma were recorded (Figure 7D). In control conditions, this stimulus generated a 0.82 ± 0.11 mV uEPSP and a 7.1% ± 0.5% $\Delta G_{uEPSP}/G_{sat}$ (n = 20/13 spines/cells) (Figure S4). In the presence of apamin, the uEPSP evoked was ~72% larger (1.41 ± 0.14 mV, $p < 0.05$) and $\Delta[Ca]_{uEPSP}$ was ~98% larger ($\Delta G_{uEPSP}/G_{sat}$ = 14.0% ± 2.1%, n = 15/5 spines/cells, $p < 0.05$ compared with control) than in control conditions (Figure S4A). Application of SNX resulted in a comparable increase in uEPSP and $\Delta[Ca]_{uEPSP}$ (uEPSP = 1.34 ± 0.20 mV; $\Delta G_{uEPSP}/G_{sat}$ = 12.9% ± 1.2%; n = 16/7 spines/cells; $p < 0.05$ compared to control) (Figure S4B), whereas TTX increased $\Delta[Ca]_{uEPSP}$ ($\Delta G_{uEPSP}/G_{sat}$ = 14.9% ± 1.5%; n = 7/3 spines/cells; $p < 0.05$ compared with control) without affecting uEPSP amplitude (0.96 ± 0.10 mV) (Figure S4C). These results confirm that, under conditions of normalized glutamate exposure, the net effect of SK and $CaV_{2.3}$ channel opening is to dampen the uEPSP and $\Delta[Ca]_{uEPSP}$, whereas VGSCs act to reduce $\Delta[Ca]_{uEPSP}$ without affecting synaptic potentials (summary data in Figures 7D–7F).

$CaV_{2.3}$ Ca Microdomains Are Preserved at High Temperature

The kinetics and gating of ion channels and the kinetics of Ca extrusion from the cytoplasm are highly temperature dependent, and thus, the contributions of $CaV_{2.3}$ VSCCs to synaptic signals may be different at physiological temperatures. Therefore, we repeated our analysis at 33°C using the photobleaching approach to set laser power. At this temperature and in control conditions, standardizing the uncaging laser power to achieve $\Delta R/R_0$ of ~40% resulted in uEPSP = 0.81 ± 0.13 mV and $\Delta[Ca]_{uEPSP}$ = 10.6% ± 1.6% $\Delta G_{uEPSP}/G_{sat}$ (n = 12/6 spines/cells) (Figure 7G). In the presence of apamin, the uEPSP and $\Delta G_{uEPSP}/G_{sat}$ increased to 1.62 ± 0.19 mV and 18.1% ± 2.0%, respectively ($p < 0.05$; n = 12/4 spines/cells) (Figure 7H). SNX application resulted in a larger uEPSP (1.81 ± 0.20 mV, $p < 0.5$) without an increase of $\Delta[Ca]_{uEPSP}$ ($\Delta G_{uEPSP}/G_{sat}$ = 11.0 ± 1.3; n = 14/9 spines/cells) (Figure 7I). Coapplication of SNX and apamin resulted

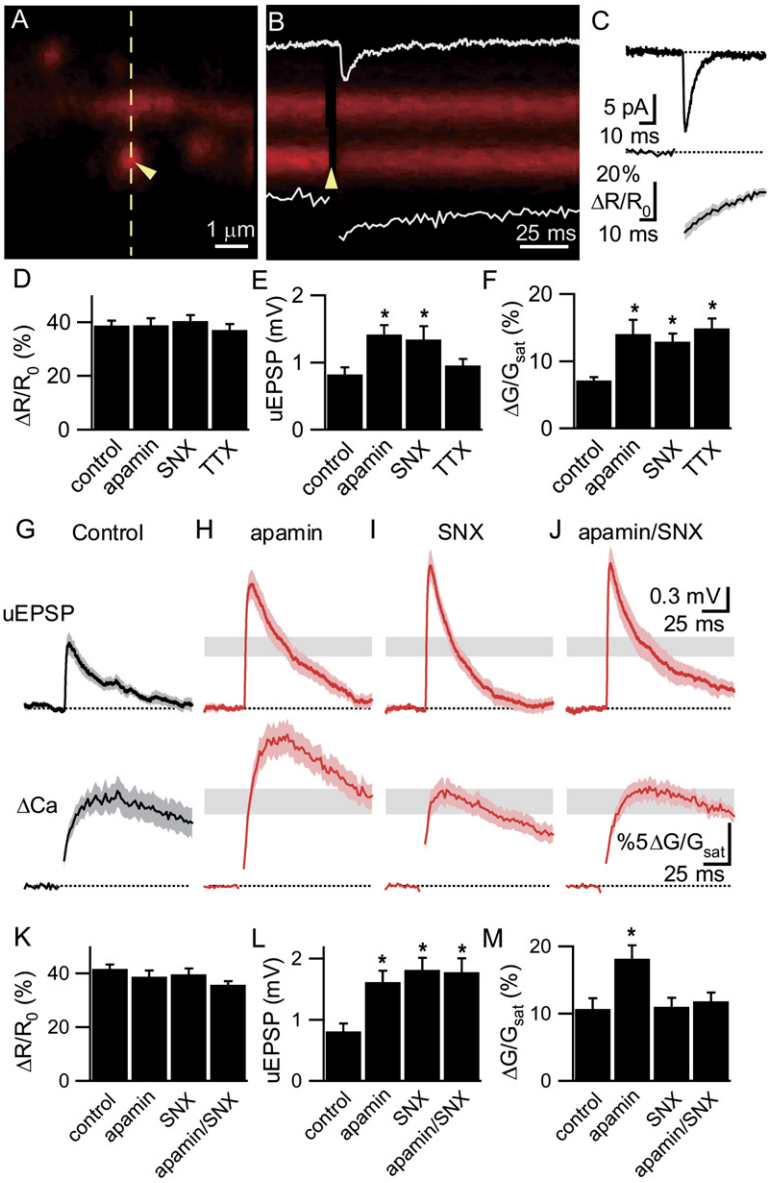

Figure 7. $CaV_{2.3}$ Channel Activity Is Necessary for SK-Dependent Regulation of the Synaptic Potentials and Spine Head Ca Transients at Near-Physiological Temperatures

(A) 2PLSM image of a spiny region of an apical dendrite of a CA1 hippocampal pyramidal neuron filled with 10 μM Alexa 594 (red fluorescence) and 300 μM of the Ca indicator Fluo-5F (green fluorescence).

(B) Red fluorescence in the spine head (sp) and neighboring dendrite (den) measured over the region indicated by the dashed line in (A). The arrowheads in (A) and (B) indicate the location and timing, respectively, of a 500 μs pulse of 725 nm laser light directed at the spine head. The white traces show the uEPSC (top) (amplitude 16.1 pA) and the red fluorescence signal (bottom) (38% bleaching) in the spine head.

(C) uEPSC (top) and bleaching of the red fluorescence signal (bottom) measured using the same laser power.

(D–F) Summary of amplitudes of $\Delta R/R_0$ (D), uEPSP (E), and $\Delta G_{uEPSP}/G_{sat}$ (F) in control conditions, or in the presence of apamin, SNX, or TTX. Traces are shown in Figure S4. (*) indicates $p < 0.05$ compared with control conditions.

(G–J) uEPSP (top) and $\Delta G_{uEPSP}/G_{sat}$ (bottom) measured at elevated temperature in control conditions (G) (black traces) or in the presence of apamin (H), SNX (I), or SNX/apamin (J) (red traces). The range of amplitudes (±SEM) of the uEPSP and $\Delta G_{uEPSP}/G_{sat}$ measured in control conditions is shown in the gray shaded bars.

(K–M) Summary of amplitudes of the $\Delta R/R_0$ (K), uEPSP (L), and $\Delta G_{uEPSP}/G_{sat}$ (M) in control conditions or in the presence of apamin, SNX, or SNX/apamin measured at elevated temperature. 1% $\Delta G/G_{sat}$ corresponds to 5.5 nM Δ[Ca] (see Experimental Procedures). (*) indicates $p < 0.05$ compared with control conditions.

in synaptic signals that resembled those seen in the presence of SNX alone (uEPSP = 1.77 ± 0.23, $\Delta G_{uEPSP}/G_{sat}$ = 11.8 ± 1.3; n = 14/4 spines/cells) (Figure 7J), confirming that activation of $CaV_{2.3}$ VSCCs is necessary for the effects of apamin on synaptic signals at near-physiological temperatures. In contrast to what was seen at room temperature, these results indicate that in the presence of apamin, and possibly in control conditions, SNX-sensitive channels contribute a large fraction of the evoked Ca influx.

DISCUSSION

Here we use 2-photon uncaging of glutamate to mimic synaptic activation of individual spines and examine the role of voltage-sensitive Ca and Na channels in shaping evoked signals. We show that the amplitude of uncaging-evoked potentials and spine head Ca signals are influenced by the activity of multiple classes of ion channels. We find that the magnitude of these signals do not directly reflect the number of open AMPA- and NMDA-type glutamate receptors, but they can be boosted or dampened by the activity of voltage-gated and Ca-dependent channels in the spine head and dendrite. Furthermore, Ca transients within the spine head and synaptic potentials at the soma are not necessarily regulated in parallel, and each parameter is differentially dependent on the complement of available ion channels. Therefore, the selective regulation of individual VSCC subclasses, of voltage-gated Na channels, or of Ca-activated K-channels can separately adjust the electrical and biochemical consequences of synaptic activity.

Multiple Classes of VSCCs in Thin Apical Dendrites and Their Dendritic Spines

In this study we identify VSCC subclasses that are present in thin dendrites and dendritic spines of CA1 pyramidal neurons by probing their activation with single bAPs and trios of bAPs (Figures 2 and 3 and Figure S2). All analyses were performed in the proximal 150 μm of secondary and tertiary dendrites in acute slices prepared from P15–P18 C57/Blk6 mice. VSCCs are classified according to their pharmacological sensitivity and are referred to by the $CaV_{X.X}$ nomenclature (Catterall et al., 2005), although we have not independently confirmed the molecular identity of the channels. In order to simplify the analysis and avoid possible nonlinear effects of SK channel activation on $\Delta[Ca]_{bAP}$, apamin is included in these experiments.

We identified a combination of VSCC antagonists (nimodipine, CTX-MVIIC, SNX, and mibefradil) that does not interfere with bAP propagation into dendrites and spines, but prevents all bAP-evoked Ca signals. By selectively withdrawing pharmacological antagonists from this cocktail, we identify the contribution of each channel type to $\Delta[Ca]_{bAP}$. We find that CaV_3 VSCCs are present in both the dendritic shaft and in the spine, as evidenced by the presence of a Ca transient that is blocked by mibefradil but is insensitive to nimodipine, CTX-MVIIC, and SNX. Furthermore, we find a SNX-sensitive contribution to $\Delta[Ca]_{bAP}$ that is present in dendritic spines, but absent in the dendritic shaft. Since the high-input impedance of the spine head ensures that it follows the dendritic membrane voltage during a bAP (Koch and Zador, 1993; Segev and Rall, 1988), the selective effects of SNX on $\Delta[Ca]_{bAP}$ in the spine demonstrates that $CaV_{2.3}$ channels are located on the spine and not on the dendrite. Lastly, we show that pharmacologically isolated $CaV_{1.2/1.3}$ and $CaV_{2.2}$ VSCCs are activated by bAPs in both the spine and the dendrite, whereas $CaV_{2.1}$ type channels are absent from both compartments.

Many studies have shown that voltage-gated conductances are found in spines and dendrites of hippocampal pyramidal neurons (Mills et al., 1994; Sabatini and Svoboda, 2000; Yasuda et al., 2003) and that VSCCs in the dendrite can be activated by large synaptic depolarizations (Magee et al., 1995; Magee and Johnston, 1995; Markram and Sakmann, 1994; Schiller et al., 1998). However, to our knowledge the activation of voltage-sensitive conductances within an active spine head by unitary synaptic stimuli has not been previously demonstrated. Moreover, the complement of channels present in spines and dendrites may be species- and preparation-dependent and is likely to vary by position in the dendritic arbor. Direct electrical recordings from primary apical dendrites of rat CA1 pyramidal neurons have identified VGSCs, dihydropyridine-sensitive ($CaV_{1.2/1.3}$) VSCCs, and Ni-sensitive VSCCs that may represent $CaV_{2.3}$ or CaV_3 (Magee et al., 1995). In these studies CTX-MVIIC-sensitive ($CaV_{2.1/2.2}$) VSCCs were found only at the soma and not in dendrites. Similarly, optical analysis of Ca signaling in spines and dendrites of rat CA1 pyramidal neurons has shown that the bulk of bAP-evoked Ca influx is carried by Ni-sensitive, high-threshold-activated VSCCs that are likely to represent $CaV_{2.3}$ (Sabatini and Svoboda, 2000; Yasuda et al., 2003). Dihydropyridine-sensitive ($CaV_{1.2/1.3}$) VSCCs were found to make only a small contribution to $\Delta[Ca]_{bAP}$ in the dendrite. In the spine, Ca influx through $CaV_{1.2/1.3}$ was not detectable, but did trigger a CAMKII-dependent reduction in $\Delta[Ca]_{bAP}$ (Yasuda et al., 2003).

Nonlinear Signaling Cascades Regulate Spine Head Ca

Our studies demonstrate the existence of nonlinear, VSCC-dependent signaling cascades that regulate bAP and synaptically evoked Ca influx in dendritic spines. This conclusion is inescapable given that when certain classes of VSCCs are blocked, $\Delta[Ca]_{bAP}$ and $\Delta[Ca]_{uEPSP}$ were larger in the spine head than when all VSCCs are available (Figure 4 and Figures S2–S4). Thus, the activation of one Ca channel dampens Ca influx through other VSCCs or NMDARs. The presence of nonlinear interactions between Ca channels is further revealed by comparison of the linear sum of the pharmacologically isolated bAP-evoked Ca influxes through $CaV_{1.2/1.3}$, $CaV_{2.1}$, $CaV_{2.2}$, $CaV_{2.3}$, and CaV_3 VSCCs to the smaller $\Delta[Ca]_{bAP}$ measured in control conditions (Figure S3). Because of the experiment design, this sublinear interaction cannot be explained by overlapping pharmacological sensitivity of VSCCs or by saturation of the Ca indicator, which is maintained in the lower 10% of its dynamic range. The nonlinear effects of VSCC blockade on $\Delta[Ca]_{bAP}$ in the spine head may be due to local activation of apamin-insensitive Ca-dependent K-channels (such as BK) or from cross-subtype Ca-dependent inactivation of VSCCs. Alternatively, current flux through a subset of VSCCs may be sufficient to directly alter the waveform of the bAP in the dendrite and thereby alter the activation of other VSCC classes.

$CaV_{2.3}$ VSCCs Are Selectively Coupled to SK Channels

The opening of SK channels during synaptic activity normally repolarizes the spine and promotes the reblock of NMDARs with Mg (Ngo-Anh et al., 2005). Therefore, blocking SK channels boosts the EPSP and enhances NMDAR-dependent Ca influx, increasing the amplitude of spine head Ca transients. This effect likely explains the reduced threshold for LTP induction found in the presence of apamin (Stackman et al., 2002). We demonstrate here that the apamin-induced enhancement of the uEPSP and $\Delta[Ca]_{uEPSP}$ are blocked by a cocktail of VSCC and mGluR antagonists, indicating that Ca influx through NMDARs is not sufficient to trigger SK channel activation.

We find that application of SNX to block $CaV_{2.3}$ VSCCs, the high-voltage activated Ca channels with the lowest activation threshold, qualitatively and quantitatively mimics the effects of apamin. Furthermore, in the presence of SNX, additional application of apamin has no effect on these signals, suggesting that $CaV_{2.3}$ VSCCs are the source of Ca that activates SK channels. Since evoked

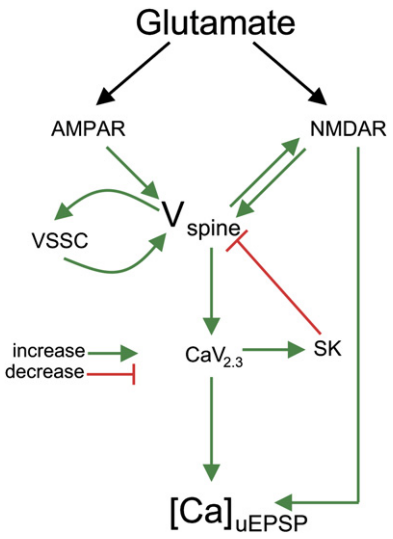

Figure 8. A Model of the Regulation of Spine Head Ca Transients by Ionotropic Glutamate Receptors, Voltage-Gated Na and Ca Channels, and SK Channels

Glutamate release activates AMPARs and NMDARs in the spine. AMPAR opening increases the potential in the spine (V_{spine}), enhancing current flow through NMDARs by relief of Mg block. The local depolarization also activates a variety of voltage-sensitive channels that contribute additional depolarization or Ca entry into the spine. Ca through $CaV_{2.3}$ channels specifically activates SK channels that repolarize the spine and terminate NMDAR signaling. Positive and negative interactions are shown by green and red lines, respectively.

spine head Ca concentrations are enhanced in the presence of SNX, failure of SK activation in this condition indicates that average ("bulk") [Ca] in the spine head is irrelevant for SK opening. Instead, SKs are likely to be located and activated within Ca signaling microdomains of $CaV_{2.3}$ VSCCs. Selective activation of SKs by a VSCC subclass ($CaV_{1.2/1.3}$) has been described previously in the soma of rat hippocampal pyramidal neurons (Marrion and Tavalin, 1998).

In the presence of antagonists of $CaV_{2.2}$, apamin robustly boosts $\Delta[Ca]_{uEPSP}$ and uEPSP amplitudes, indicating that their activity is not necessary for SK opening. The role of $CaV_{1.2/1.3}$ in the activation of SKs is less clear. In the presence of nimodipine, the amplitude of the uEPSP is the same as in control conditions and is enhanced by the application of apamin, suggesting that $CaV_{1.2/1.3}$ is not necessary for the SK-mediated depression of the uEPSP. However, in the presence of nimodipine and apamin, $\Delta[Ca]_{uEPSP}$ is intermediate to that measured in control conditions and in apamin alone, and is statistically indistinct from both. Thus, our data cannot rule out the possibility that $CaV_{1.2/1.3}$ and $CaV_{2.3}$ VSCCs act cooperatively to activate SKs and regulate $\Delta[Ca]_{uEPSP}$. Lastly, we find that the opening of VGSCs is necessary for the effects of apamin on the uEPSP and $\Delta[Ca]_{uEPSP}$. In the presence of TTX, the uEPSP is unaffected but $\Delta[Ca]_{uEPSP}$ is increased, and apamin application has no additional effect on either parameter. A sample explanation of these effects is that VGSC opening promotes the activation of $CaV_{2.3}$ VSCCs that, in turn, admit Ca that opens SK channels (Figure 8).

Conclusions

Our study demonstrates that unitary stimuli that generate submillivolt potentials at the soma are shaped by the activation of multiple classes of ion channels. $CaV_{2.3}$ channels are found in spines and not in the dendrite, suggesting that synaptic stimulation is capable of depolarizing the spine by the many tens of millivolts necessary to activate these channels. Additionally, $CaV_{2.3}$ VSCCs specifically activate SK channels that regulate synaptic signals. Previously, the distance between SK channels and their activating Ca source had been estimated at 25–50 nm (Ngo-Anh et al., 2005). These data, along with the lack of a detectable synaptically evoked Ca accumulation outside of the spine, indicate that the feedback loop described here is contained entirely within the active spine. Furthermore, we find that changes in the activity of voltage- and Ca-dependent ion channels alter synaptically evoked potentials by nearly a factor of 2, a degree of modulation similar to that seen with the induction of LTP. Thus, by altering synaptically evoked Ca transients and potentials, regulation of ion channels in the spine head provides a potentially powerful glutamate receptor-independent mechanism for controlling the induction and expression of synaptic plasticity.

EXPERIMENTAL PROCEDURES

Slice Preparation

Animals were handled in accordance with Federal guidelines and protocols approved by Harvard University. Hippocampal slices were prepared from C57/Blk6 mice from P15–P18. Animals were anesthetized by inhalation of isoflurane. The cerebral hemispheres were quickly removed and placed into cold choline-based artificial cerebrospinal fluid (choline-ACSF) containing 25 mM $NaHCO_3$, 1.25 mM NaH_2PO_4, 2.5 mM KCl, 7 mM $MgCl_2$, 25 mM glucose, 1 mM $CaCl_2$, 110 mM choline chloride, 11.60 mM ascorbic acid, and 3.10 mM pyruvic acid, and equilibrated with 95% O_2/5% CO_2. Tissue was blocked and transferred into a slicing chamber containing choline-ACSF. Transverse hippocampal slices (300 μm) were cut with a Leica VT1000s (Leica Instruments, Nussloch, Germany) and transferred into a holding chamber containing ACSF consisting of 125 mM NaCl, 2.5 mM KCl, 21.4 mM $NaHCO_3$, 1.25 mM NaH_2PO_4, 2.0 mM $CaCl_2$, 1.0 mM $MgCl_2$, and 11.1 mM glucose and were equilibrated with 95% O_2/5% CO_2. Slices were incubated at 35°C for 30–45 min and then left at room temperature until recordings were performed.

Electrophysiology

Whole-cell recordings were obtained from CA1 pyramidal cells visualized under IR-DIC. Patch pipettes (open pipette resistance, 2.5–4.5 MΩ) were filled with a solution containing 140 mM $KMeSO_4$, 8 mM NaCl, 1 mM $MgCl_2$, 10 mM HEPES, 5 mM MgATP, and 0.4 mM Na_2GTP (pH 7.3). In experiments where bAP activation of VSCCs was measured, 150 μM Fluo-5F (Molecular Probes, K_D = ~550 nM at 35°C (Brenowitz et al., 2006) and 1.1 μM at room temperature [Stephan Brenowitz, unpublished data] in K-based intracellular) and 5 μM Alexa 594 were added to the internal solution. In experiments where uncaging-evoked responses were measured, 300 μM Fluo-5F and 10 μM Alexa 594 were used. Recordings were made using an Axoclamp 200B amplifier (Axon Instruments, Union City, CA). Data were filtered at 2 or 5 kHz and sampled at 10 kHz. For recordings measuring

VSCC activation by bAPs, cells were maintained near −70 mV. To measure uncaging-evoked currents and adjust laser power, cells were voltage-clamped at −60 mV. In all recordings the series resistance (measured with a 5 mV hyperpolarizing pulse in voltage-clamp) was less than 20 MΩ and uncompensated. Recordings were performed at room temperature or at 33°C as indicated in the text and within 7 hr of slice preparation.

Pharmacology

The following pharmacological agents at the following final concentrations were used as described in the text: 0.1 μM apamin (Calbiochem, La Jolla, CA), 20 μM CPP (Tocris Cookson, Ellisville, MO), 40 μM MK-801 (Tocris Cookson, Ellisville, MO), 10 μM D-serine (Sigma, St. Louis, MO), 10 μM mibefradil (Sigma, St. Louis, MO), 0.3 μM SNX-482 (Peptides International, Louisville, KY), 1 μM CTX-MVIIC (Peptides International, Louisville, KY), 1 μM CTX-GVIA (Peptides International, Louisville, KY), 0.3 μM AgTx-IVA (Sigma, St. Louis, MO), 1 μM TTX (Sigma, St. Louis, MO), 1 μM MPEP (Tocris Cookson, Ellisville, MO), 100 μM CPCCOEt (Tocris Cookson, Ellisville, MO), and 20 μM nimodipine (Sigma, St. Louis, MO). All reagents were dissolved in distilled water except MPEP, CPCCOEt, and nimodipine, which were dissolved in DMSO. Stock solutions in water were diluted in ACSF to a final dilution of 1:1000 on the day of the experiment except for peptide toxins, which were diluted 1:100. Stock solutions in DMSO were diluted in ACSF to a final dilution of 1:10,000 on the day of the experiment. In all experiments 10 μM D-serine was included in the ACSF.

2-Photon Uncaging and Imaging

Combined 2-photon uncaging of MNI-glutamate and 2-photon imaging was performed using a custom microscope (Bloodgood and Sabatini, 2005; Carter and Sabatini, 2004; Ngo-Anh et al., 2005). MNI-glutamate (Tocris Cookson, Ellisville, MO) was included in the bath at 5 mM or 3.75 mM for experiments conducted at room temperature or 33°C, respectively. MNI-glutamate was uncaged using 500 μs pulses of 725 nm light. Alexa Fluor 594 and Fluo-5F were excited at a wavelength of 840 nm and stimulus-evoked changes in fluorescence were quantified as increases in green (Fluo-5F) fluorescence from baseline divided by resting red (Alexa Fluor 594) fluorescence (ΔG/R). This method provides quantification that is insensitive to small changes in resting Ca and independent of spine volume (Sabatini et al., 2002). G/R was also measured in saturating Ca (G_{sat}/R) for each dye combination and batch of intracellular solution by imaging a sealed pipette filled with equal volumes of 1 M $CaCl_2$ and the internal solution. ΔG/R measurements were divided by G_{sat}/R, giving the reported fluorescence measurement of $\Delta G/G_{sat}$. The standard use of $\Delta G/G_{sat}$ allows for comparison of data collected on multiple microscopes or by multiple researchers. Furthermore, $\Delta G/G_{sat}$ is insensitive to the concentration of Alexa Fluor 594 and insensitive to relative collection efficiencies of red and green photons. G_{sat}/R was measured for each batch of internal solution and on a weekly basis.

In all experiments, before each uncaging pulse, an image of the spine was acquired and automatically aligned with a reference image of the spine. Shifts in the spine location were calculated by crosscorrelation of the images and were cancelled by addition of electronic offsets to the scan mirrors, thereby stabilizing the uncaging location (Carter and Sabatini, 2004). In the majority of experiments (Figure 1 and Figures 4–6), for each spine analyzed the uncaging laser power was adjusted to evoke a 10–15 pA uEPSC. In these experiments, test pulses were first delivered around the perimeter of the spine to determine the optimal site of uncaging. The laser power was adjusted to evoke a current of 10–15 pA at that location. Subsequently, each spine was stimulated five to ten times (interstimulus interval 15 s) at that location and the uEPSCs averaged. The experiment was repeated in current clamp and the uEPSP and uEPSP-evoked Ca transient were recorded.

Subsets of experiments (Figure 7 and Figure S4) were performed in which the power of the uncaging pulse was set to bleach ~40% of the red fluorophore in the spine. Bleaching is a function of the effective laser power and thus provides a readout of power delivered to the spine that is independent of the depth of the spine analyzed or local inhomogeneities affecting the tissue's index of refraction (see Supplemental Experimental Procedures). Furthermore, it provides a measure of power that is independent of electrophysiological responses. In these experiments, the uncaging laser was directed at the center of the spine head and the pulse adjusted to achieve the proper level of bleaching of the red fluorophore. Using this laser power, test pulses were delivered around the perimeter of the spine head to determine the optimal site of uncaging. In current clamp, the spine was stimulated five to ten times at the optimal location to obtain the average response.

Spines on secondary and tertiary apical dendrites within 150 μm of the soma were selected for analysis. These proximal sites were chosen to ensure propagation of the bAP to the site of interest and to improve the ability to voltage-clamp potentials in the spine.

Data Analysis

Off-line data analysis was performed using custom software written in Igor Pro (Wavemetrics) and MATLAB. $\Delta G_{bAP}/G_{sat}$ evoked by a single AP was determined by averaging $\Delta G_{bAP}/R$ for 30 ms starting 4 ms after the generation of the bAP and then dividing by G_{sat}/R measured in the same batch of internal solution. $\Delta G_{bAP}/G_{sat}$ evoked by a triplet of APs was determined by averaging $\Delta G_{bAP}/R$ for 30 ms starting 4 ms after the generation of the third bAP. $\Delta G_{uEPSP}/G_{sat}$ was determined by averaging $\Delta G_{uEPSP}/R$ for 100 ms starting 20 or 10 ms after the uncaging pulse for measurements made at room temperature or 33°C, respectively, and subsequently dividing by G_{sat}/R. Stimulus-evoked increases in free calcium (Δ[Ca]) were estimated by

$$\frac{\Delta G/R}{G_{sat}/R} = \frac{\Delta[CaB]}{B_{total}} \approx \frac{\Delta[Ca]}{K_D}$$

where *CaB* is the buffer bound to calcium, B_{total} is the added buffer, and *Ca* is the free calcium. This linear estimate is valid because the indicator was used in the lower end of ~10%–15% of its dynamic range. The uEPSP peak was determined by averaging the potential from 0.5 ms before to 2.5 ms after the uEPSP maximum value. Similarly, the uEPSC peak was determined by averaging the current amplitude from 0.2 ms before to 1.8 ms after the minimum uEPSC value. All data are expressed as the average ± SEM unless otherwise indicated. In the figures, average traces are shown as the mean (line) ± the SEM (shaded regions) with the exception of Figure S1, in which the SD is shown.

A two-tailed t test was used to determine significance of differences in $\Delta G_{bAP}/G_{sat}$, uEPSP, and $\Delta G_{uEPSP}/G_{sat}$ across conditions. $p < 0.05$ was considered significant. Error propagation and estimation for the calculated sums or differences of $\Delta G_{bAP}/G_{sat}$ (Figures S2 and S3) were done by assuming independent normal distributions of the means in each condition and setting the variance of the new distribution to the sum of variances of the component distributions. In Figure S1, the expected SEM expressed as a percentage of the mean for parameter *x* was calculated from

$$SEM_x(n) = 100\frac{\sigma_x}{\langle x\rangle\sqrt{n}}$$

where *n* is the number of spines analyzed and $\langle x\rangle$ and σ_x are the mean and standard deviation of *x*, respectively.

Supplemental Data

The Supplemental Data for this article can be found online at http://www.neuron.org/cgi/content/full/53/2/249/DC1/.

ACKNOWLEDGMENTS

We thank Veronica Alvarez for helpful discussions and critical reading of the manuscript. This work was funded by the Whitaker Foundation (B.L.B.) and NINDS (RO1 NS046579-01A), the McKnight Foundation, the Hellman Family Fund, and the Searle Scholars Program (B.L.S.).

Received: June 26, 2006
Revised: November 10, 2006
Accepted: December 14, 2006
Published: January 17, 2007

REFERENCES

Bloodgood, B.L., and Sabatini, B.L. (2005). Neuronal activity regulates diffusion across the neck of dendritic spines. Science *310*, 866–869.

Brenowitz, S.D., Best, A.R., and Regehr, W.G. (2006). Sustained elevation of dendritic calcium evokes widespread endocannabinoid release and suppression of synapses onto cerebellar purkinje cells. J. Neurosci. *26*, 6841–6850.

Carter, A.G., and Sabatini, B.L. (2004). State-dependent calcium signaling in dendritic spines of striatal medium spiny neurons. Neuron *44*, 483–493.

Catterall, W.A., Perez-Reyes, E., Snutch, T.P., and Striessnig, J. (2005). International union of pharmacology. XLVIII. Nomenclature and structure-function relationships of voltage-gated calcium channels. Pharmacol Rev. *57*, 411–425.

Golding, N.L., Staff, N.P., and Spruston, N. (2002). Dendritic spikes as a mechanism for cooperative long-term potentiation. Nature *418*, 326–331.

Hinkle, P.M., Shanshala, E.D., Jr., and Nelson, E.J. (1992). Measurement of intracellular cadmium with fluorescent dyes. Further evidence for the role of calcium channels in cadmium uptake. J. Biol. Chem. *267*, 25553–25559.

Hoffman, D.A., Magee, J.C., Colbert, C.M., and Johnston, D. (1997). K+ channel regulation of signal propagation in dendrites of hippocampal pyramidal neurons. Nature *387*, 869–875.

Johnston, D., Williams, S., Jaffe, D., and Gray, R. (1992). NMDA-receptor-independent long-term potentiation. Annu. Rev. Physiol. *54*, 489–505.

Koch, C., and Zador, A. (1993). The function of dendritic spines: devices subserving biochemical rather than electrical compartmentalization. J. Neurosci. *13*, 413–422.

Legendre, P., and Westbrook, P.L. (1990). The inhibition of single N-methyl-D-aspartate-activated channels by zinc ions on cultured rat neurones. J. Physiology *429*, 429–449.

Losonczy, A., and Magee, J.C. (2006). Integrative properties of radial oblique dendrites in hippocampal CA1 pyramidal neurons. Neuron *50*, 291–307.

Magee, J., Hoffman, D., Colbert, C., and Johnston, D. (1998). Electrical and calcium signaling in dendrites of hippocampal pyramidal neurons. Annu. Rev. Physiol. *60*, 327–346.

Magee, J.C. (1999). Dendritic Ih normalizes temporal summation in hippocampal CA1 neurons. Nat. Neurosci. *2*, 508–514.

Magee, J.C., and Cook, E.P. (2000). Somatic EPSP amplitude is independent of synapse location in hippocampal pyramidal neurons. Nat. Neurosci. *3*, 895–903.

Magee, J.C., and Johnston, D. (1995). Synaptic activation of voltage-gated channels in the dendrites of hippocampal pyramidal neurons. Science *268*, 301–304.

Magee, J.C., Christofi, G., Miyakawa, H., Christie, B., Lasser-Ross, N., and Johnston, D. (1995). Subthreshold synaptic activation of voltage-gated Ca2+ channels mediates a localized Ca2+ influx into the dendrites of hippocampal pyramidal neurons. J. Neurophysiol. *74*, 1335–1342.

Mainen, Z.F., Maletic-Savatic, M., Shi, S.H., Hayashi, Y., Malinow, R., and Svoboda, K. (1999). Two-photon imaging in living brain slices. Methods *18*, 231–239.

Majewska, A., Brown, E., Ross, J., and Yuste, R. (2000). Mechanisms of calcium decay kinetics in hippocampal spines: role of spine calcium pumps and calcium diffusion through the spine neck in biochemical compartmentalization. J. Neurosci. *20*, 1722–1734.

Markram, H., and Sakmann, B. (1994). Calcium transients in dendrites of neocortical neurons evoked by single subthreshold excitatory postsynaptic potentials via low-voltage-activated calcium channels. Proc. Natl. Acad. Sci. USA *91*, 5207–5211.

Marrion, N.V., and Tavalin, S.J. (1998). Selective activation of Ca2+-activated K+ channels by co-localized Ca2+ channels in hippocampal neurons. Nature *395*, 900–905.

McDonough, S.I., and Bean, B.P. (1998). Mibefradil Inhibition of T-Type Calcium Channels in Cerebellar Purkinje Neurons. Mol. Pharmacol. *54*, 1080–1087.

Metz, A.E., Jarsky, T., Martina, M., and Spruston, N. (2005). R-type calcium channels contribute to afterdepolarization and bursting in hippocampal CA1 pyramidal neurons. J. Neurosci. *25*, 5763–5773.

Mills, L., Niesen, C., So, A., Carlen, P., Spigelman, I., and Jones, O. (1994). N-type Ca2+ channels are located on somata, dendrites, and a subpopulation of dendritic spines on live hippocampal pyramidal neurons. J. Neurosci. *14*, 6815–6824.

Nevian, T., and Sakmann, B. (2004). Single spine Ca2+ signals evoked by coincident EPSPs and backpropagating action potentials in spiny stellate cells of Layer 4 in the juvenile rat somatosensory barrel cortex. J. Neurosci. *24*, 1689–1699.

Ngo-Anh, T.J., Bloodgood, B.L., Lin, M., Sabatini, B.L., Maylie, J., and Adelman, J.P. (2005). SK channels and NMDA receptors form a Ca2+-mediated feedback loop in dendritic spines. Nat. Neurosci. *8*, 642–649.

Oertner, T.G., Sabatini, B.L., Nimchinsky, E.A., and Svoboda, K. (2002). Facilitation at single synapses probed with optical quantal analysis. Nat. Neurosci. *5*, 657–664.

Randall, A.D., and Tsien, R.W. (1997). Contrasting biophysical and pharmacological properties of T-type and R-type calcium channels. Neuropharmacology *36*, 879–893.

Regehr, W.G., and Atluri, P.P. (1995). Calcium transients in cerebellar granule cell presynaptic terminals. Biophys. J. *68*, 2156–2170.

Sabatini, B.L., and Svoboda, K. (2000). Analysis of calcium channels in single spines using optical fluctuation analysis. Nature *408*, 589–593.

Sabatini, B.L., Oertner, T.G., and Svoboda, K. (2002). The life cycle of Ca(2+) ions in dendritic spines. Neuron *33*, 439–452.

Schiller, J., Schiller, Y., and Clapham, D.E. (1998). NMDA receptors amplify calcium influx into dendritic spines during associative pre- and postsynaptic activation. Nat. Neurosci. *1*, 114–118.

Segev, I., and Rall, W. (1988). Computational study of an excitable dendritic spine. J. Neurophysiol. *60*, 499–523.

Stackman, R.W., Hammond, R.S., Linardatos, E., Gerlach, A., Maylie, J., Adelman, J.P., and Tzounopoulos, T. (2002). Small conductance Ca2+-activated K+ channels modulate synaptic plasticity and memory encoding. J. Neurosci. *22*, 10163–10171.

Stocker, M., Krause, M., and Pedarzani, P. (1999). An apamin-sensitive Ca2+-activated K+ current in hippocampal pyramidal neurons. Proc. Natl. Acad. Sci. USA *96*, 4662–4667.

Wei, D.-S., Mei, Y.-A., Bagal, A., Kao, J.P.Y., Thompson, S.M., and Tang, C.-M. (2001). Compartmentalized and binary behavior of terminal dendrites in hippocampal pyramidal neurons. Science *293*, 2272–2275.

Westbrook, G.L., and Mayer, M.L. (1987). Micromolar concentrations of Zn2+ antagonize NMDA and GABA responses of hippocampal neurons. Nature *328*, 640–643.

Yasuda, R., Sabatini, B.L., and Svoboda, K. (2003). Plasticity of calcium channels in dendritic spines. Nat. Neurosci. *6*, 948–955.

Yuste, R., and Denk, W. (1995). Dendritic spines as basic functional units of neuronal integration. Nature *375*, 682–684.

Neuron, volume 53

Supplemental Data

Nonlinear Regulation of Unitary Synaptic Signals by CaV2.3 Voltage-Sensitive Calcium Channels Located in Dendritic Spines

Brenda L. Bloodgood and Bernardo L. Sabatini

Supplemental Experimental Procedures

Using bleaching of a fluorophore to standardize power delivery to the spine

The laser power for 2-photon excitation delivered to a spine within a brain slice depends on many factors. These include the depth of the spine within the slice, which influences what fraction of the light is scattered or absorbed en route to the focal point, and inhomogeneity in the index of refraction of the tissue, which influences the amount of power delivered to the spot and the volume over which this power spreads. Inhomogeneities in index of refraction along the light path to the spine due to the presence of cell bodies, axons, blood vessels, and other membrane-bound cellular structure are impossible to measure during the experiment. Therefore, in order to deliver a constant amount of power independent of these variables it is necessary to use information from a power-sensitive process that occurs at the spine of interest. This can be accomplished by adjusting power to photoactive or photobleach a constant fraction of fluorophore within the spine. Although setting laser power by photoactivation of a caged fluorophore is in principal an elegant approach, it is not feasible to implement in the current study because all commercially caged fluorophores overlap spectrally with Fluo-5F and Alexa Fluo-594.

We used photobleaching of Alexa Fluo-594 in the spine of interest to set the uncaging laser power. Laser power is adjusted to achieve bleaching of a set fraction of the Alexa Fluor-594 in the spine. In our study uncaging laser pulse duration is kept constant at 500 μs. Since we use the fractional loss of red fluorescence to set laser power, this method is insensitive to changes in the optical properties of the microscope such as collection efficiency of photons and amplifier gain. Furthermore, since fractional bleaching depends only on laser power delivered at the spine and the properties of the fluorophore (see below), this approach can be used to normalize power delivery across microscopes and laboratories.

Under 2PLSM the red fluorescence (R) emitted from a spine is given by

$$R = k \int_{V_{psf}} P_i^2(x,y,z) C(x,y,z) dxdydz \qquad (1)$$

where R is the intensity of red fluorescence and k is a constant that reflects the 2-photon cross-section of the fluorophore, the quantum efficiency of the fluorophore, the collection efficiency of the microscope, and the gain of the photodetectors and amplifiers. $P_i(x,y,z)$ is the power of the imaging laser delivered to the spot as a function of space and $C(x,y,z)$ is the distribution of the concentration of the fluorophore.

Assuming (assumption 1) that the volume of the spine (V_{sp}) is smaller than the volume of the excitation volume or point-spread-function of the microscope (V_{psf}), $P_i(x,y,z)$ is approximately constant inside the spine. Then equation 1 simplifies to

$$R = kP_i^2 V_{SP} C \qquad (2)$$

where C is the concentration of unbleached fluorophore in the spine. Due to the relatively poor lateral and axial resolution of 2PLSM, assumption 1 holds for the majority of spines and has been used estimate the volume of the spine head from the absolute fluorescence intensity (Holtmaat et al., 2005; Sabatini and Svoboda, 2000).

Using equation 2, before the bleaching pulse,

$$R_0 = kP_i^2 V_{SP} C_0$$

whereas after the bleaching pulse

$$R_1 = kP_i^2 V_{SP} C_1 . \qquad (3)$$

Then the fractional decrease in red fluorescence due to the bleaching pulse is

$$\frac{\Delta R}{R_0} = \frac{R_0 - R_1}{R_0} = \frac{C_0 - C_1}{C_0} = \frac{\Delta C}{C_0} \qquad (4)$$

with $\Delta C = C_0 - C_1$ and $\Delta R = R_0 - R_1$.

As expected, equation 4 indicates that the fractional decrease in red fluorescence is equal to the fractional decrease in the concentration of unbleached fluorophore within the spine. Note that assumption 1 is not necessary to derive eq 4 and is used only to simplify the notation and presentation. Note also that in the derivation of eq 4 all k, P_i, and V_{sp} terms cancel, indicating that the fluorescence ratio is insensitive to the photon collection and detection efficiency of the microscope, imaging laser power, and spine head volume, as well as the absolute concentration of fluorophore.

The relationship between bleaching of fluorophore in the spine head and laser power is given by

$$\Delta C = V_{sp}^{-1} \int_{V_{sp}} C(x,y,z) f_{bl}\left(P_{bl}(x,y,z)\right) dxdydz \qquad (5)$$

where $P_{bl}(x,y,z)$ is the power of the bleaching laser and f_{bl} is a "bleaching function" that describes the fraction of fluorophore that is bleached as a function of laser power (see below). Using again the assumption that $V_{sp} << V_{psf}$ such that $P_{bl}(x,y,z)$ is constant throughout the spine volume, eq 5 reduces to

$$\Delta C = C_0 f_{bl}\left(P_{bl}\right)$$

or, rearranging and combining with eq 4,

$$\frac{\Delta R}{R} = \frac{\Delta C}{C_0} = f_{bl}(P_{bl}) \qquad (6)$$

This gives the desired result that the fraction of fluorophores bleached is strictly a function of the power delivered to the spine and is independent of the imaging characteristics of the microscope and absolute concentration of fluorophore.

f_{bl} has been estimated for several common synthetic fluorophores under 2-photon excitation (reviewed in Svoboda and Yasuda, 2006) and has been shown to be dominated by the second and third powers of laser intensity (Koester et al., 1999; Patterson and Piston, 2000). Therefore,

$$f_{bl} \approx \alpha P_{bl}^2 + \beta P_{bl}^3 \qquad (7)$$

And, combining eqs 6 and 7, we find that

$$\frac{\Delta R}{R_0} \approx \alpha P_{bl}^2 + \beta P_{bl}^3 .$$

Supplemental Figures

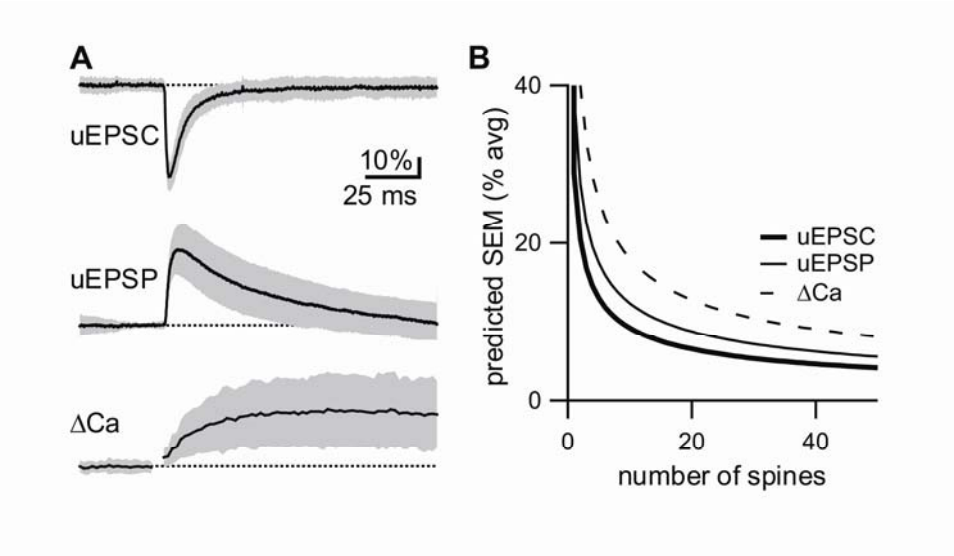

Figure S1. Estimation of the distributions of uEPSC, uEPSP, and $\Delta G_{uEPSP}/G_{sat}$ in control conditions.

(A) uEPSC (*top*), uEPSP (*middle*), and $\Delta G_{uEPSP}/G_{sat}$ (*bottom*) measured in control conditions at room temperature. Data are shown as the avgerage ± standard deviation. (n = 77/59 spines/cells, respectively).

(B) The calculated SEM for each parameter as a percentage of the mean is shown as a function of sample size. Combining data from ~ 20 spines yields an estimate of the true mean to within ~10 %.

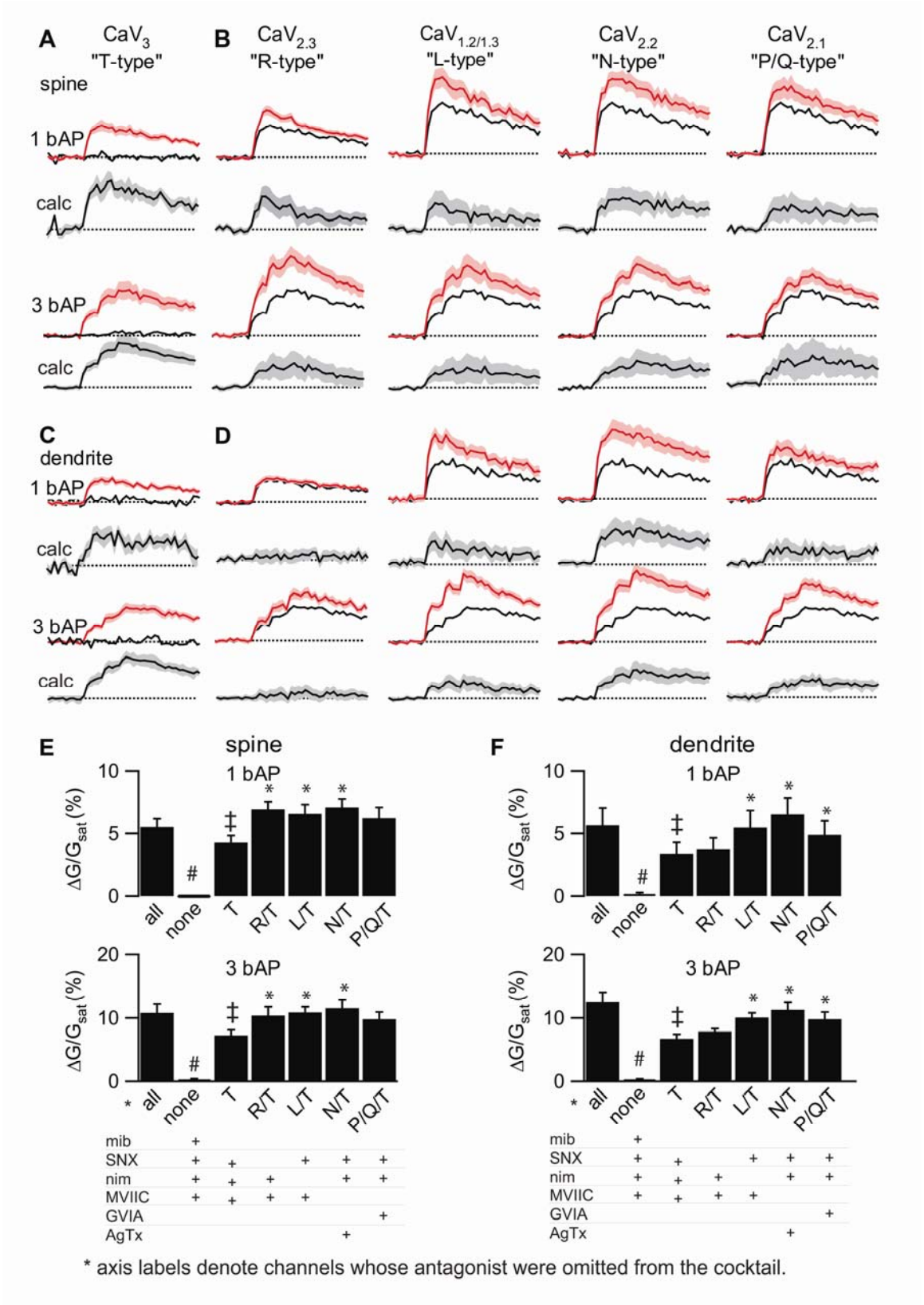
A
CaV3
"T-type"
B
CaV2.3
"R-type"
CaV1.2/1.3
"L-type"
CaV2.2
"N-type"
CaV2.1
"P/Q-type"
spine
1 bAP
calc
3 bAP
calc
C
dendrite
D
1 bAP
calc
3 bAP
calc
E
spine
1 bAP
3 bAP
ΔG/Gsat (%)
all
none
T
R/T
L/T
N/T
P/Q/T
mib
SNX
nim
MVIIC
GVIA
AgTx
F
dendrite
1 bAP
3 bAP
* axis labels denote channels whose antagonist were omitted from the cocktail.

Figure S2. Multiple and distinct sets of VSCC subclasses regulate Ca transients evoked by a trio of bAPs.

(A) $\Delta G_{bAP}/G_{sat}$ evoked by a single bAP (*top*, red trace) or a trio of bAPs (*bottom*, red trace) (50Hz) measured in the presence of nimodipine, CTX-MVIIC, SNX (*top*, red trace, n = 30/15 spines/cells) or in the additional presence of mibefradil (*top*, black trace). The latter data is replotted from Fig. 2B. As in Fig. 3A, the calculated difference between these traces (*bottom*) can be attributed to CaV_3 VSCCs.

(B) $\Delta G_{bAP}/G_{sat}$ evoked by a single bAP (*top*, red trace) or a trio of bAPs (*bottom* red trace) in the spine head in the presence of nimodipine and CTX-MVIIC (R/T-type, n = 21/11); CTX-MVIIC and SNX (L/T-type, n = 22/14); nimodipine, AgTx, and SNX (N/T-type, n = 19/9); or nimodipine, CTX-GVIA, and SNX (P/Q/T-type, n = 17/11). Comparisons are made as in Fig. 3B and 3E. The calculated differences between the black and red lines (calc) represent the additional Ca influx resulting from activation of $CaV_{1.2/1.3}$ ("L-type"), $CaV_{2.3}$ ("R-type"), $CaV_{2.2}$ ("N-type"), and $CaV_{2.1}$ ("P/Q-type") VSCCs, respectively.

(C–D) As in panels A and B for bAP-evoked fluorescence transients measured from the dendrites immediately adjacent to the analyzed spines.

(E-F) Summary of the relative amplitudes of bAP-evoked Ca transients in spines (E) and neighboring dendrites (F) in response to a single bAP (*top*) or a trio of bAPs (*bottom*) for each of the pharmacological conditions shown in (A-D). #, ‡, and * indicate statistically significant ($p<0.05$) differences compared to control, all VSCC blockers, or isolated T-type conditions, respectively.

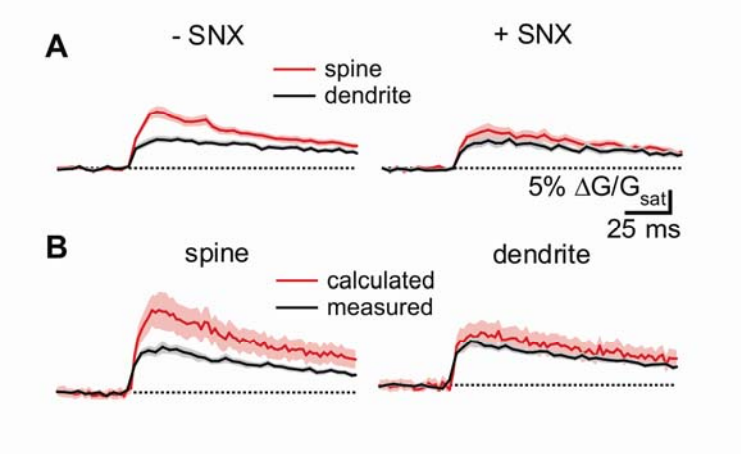

Figure S3. $CaV_{2.3}$ VSCCs are restricted to spine heads and VSCC classes interact nonlinearly to determine $\Delta[Ca]_{bAP}$

(A) $\Delta G_{bAP}/G_{sat}$ measured in the absence (*left*) and presence (*right*) of SNX. Fluorescence profiles converge after > 100 ms indicating diffusional equilibration between the two compartments also requires > 100 ms. Data are replotted from Fig. 3B and 3E.

(B) $\Delta G_{bAP}/G_{sat}$ in spines (*left*) and dendrites (*right*) evoked by a single bAP (black) and that predicted (red) from the sum of the calculated Ca signals attributed to each VSCC type shown in Fig. 3A-C and 3D-F.

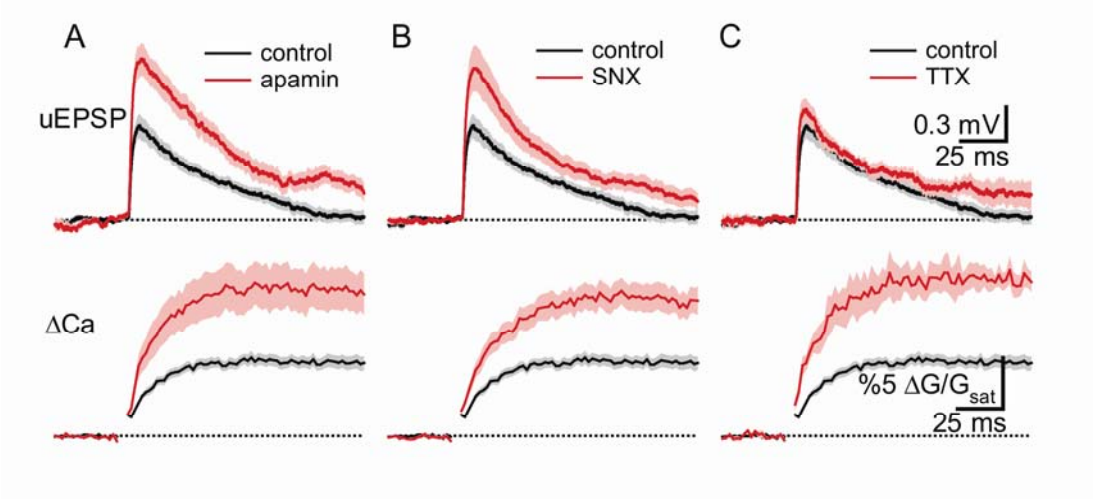

Figure S4. $CaV_{2.3}$ VSCCs and VGSC activity is necessary for SK-dependent modulation of synaptic potentials and spine head Ca transients when the stimulus strength is set by photobleaching of Alexa Fluo-594.

(A-C) uEPSP (*top*), $\alpha\nu\delta$ $\Delta G_{uEPSP}/G_{sat}$ (*bottom*) measured in control conditions (black traces, n = 20/13 spines/cells) or in the presence of apamin (A), SNX (B), or TTX (C) (red traces, n = 15/5, 16/7, 7/2 spines/cells for apamin, SNX, and TTX, respectively).

Supplemental References

Holtmaat, A. J. G. D., Trachtenberg, J. T., Wilbrecht, L., Shepherd, G. M., Zhang, X., Knott, G. W., and Svoboda, K. (2005). Transient and Persistent Dendritic Spines in the Neocortex In Vivo. Neuron *45*, 279-291.

Koester, H. J., Baur, D., Uhl, R., and Hell, S. W. (1999). Ca2+ Fluorescence Imaging with Pico- and Femtosecond Two-Photon Excitation: Signal and Photodamage. Biophys J *77*, 2226-2236.

Patterson, G. H., and Piston, D. W. (2000). Photobleaching in Two-Photon Excitation Microscopy. Biophys J *78*, 2159-2162.

Sabatini, B. L., and Svoboda, K. (2000). Analysis of calcium channels in single spines using optical fluctuation analysis. Nature *408*, 589-593.

Svoboda, K., and Yasuda, R. (2006). Principles of Two-Photon Excitation Microscopy and Its Applications to Neuroscience. Neuron *50*, 823-839.